European Polymer Journal 150 (2021) 110418

Contents lists available at ScienceDirect

European Polymer Journal

journal homepage: www.elsevier.com/locate/europolj

Improving the dielectric properties of acrylic resin elastomer with reduced graphene oxide decorated with polystyrene

Xin-Hua Gao [a], Jing-Wen Wang [a,*], Da-Nian Liu [a], Xin-Zhu Wang [a], Hou-Qing Wang [a], Lei Wei [a], Hua Ren [b]

[a] *College of Materials Science and Technology, Nanjing University of Aeronautics & Astronautics, 29 Yudao Street, Nanjing 210016, PR China*
[b] *Department of Materials Science and Engineering, Nanjing University, 22 Hankou Road, Nanjing 210093, PR China*

ARTICLE INFO

Keywords:
Acrylic resin elastomers
Modified graphene
Percolation threshold
Dielectric properties

ABSTRACT

A high performance composite based on acrylic resin elastomer (AE) with a low dielectric loss and a high dielectric constant was prepared through introducing hybrid filler of chemically reduced graphene oxide (RGO) decorated with polystyrene cationic microspheres (PS-DMC) (referred to the composite here as PS-RGO/AE). PS-DMC can not only improve the compatibility between the filler and the matrix so that the filler is uniformly dispersed in the matrix to increase the dielectric constant of the composites, but also can be used as an insulating layer to reduce leakage current and reduce the dielectric loss of the composites. The dielectric constant of 2.43 vol% PS-RGO/AE is 194 at 100 Hz, which is 2.40 times that of the 1.55 vol% RGO/AE (81). Moreover, the dielectric loss of 2.43 vol% PS-RGO/AE composite still maintains at a low level (0.29 at 100 Hz), which is lower than that of 1.55 vol% RGO/AE composite (1.16 at 100 Hz). The higher dielectric constant of PS-RGO/AE composites is attributed to enhanced micro capacitors effect and Maxwell-Wagner-Sillars effect through the uniform dispersion of PS-RGO in the AE matrix and the formation of more interfaces.

1. Introduction

Electroactive polymers can produce changes in shape and size under an applied external electric field. More and more researchers have a strong interest in electroactive polymers, which are widely used in the fields of artificial muscles, sensors, actuators, energy harvesters, super capacitors, and soft robots [1–5]. Dielectric elastomers such as acrylic resin elastomers (AE) [6], silicone rubber [7], and polyurethane elastomers [8] have the advantages of large deformation, light weight, fast response, good flexibility, high energy density, and low cost, making them stand out among electroactive polymers [9–12]. Compared with silicone rubber and polyurethane elastomers, AE is a suitable choice because of its high energy density, high breakdown strength, and large driving strain [13]. Unfortunately, dielectric elastomers usually require high electric field strength (>100 kV/mm) to obtain large driving strain, which could destroy equipment and be harmful to humans, especially in medical and biological fields [14]. Therefore, obtaining high driving strain at a low electric field is a challenge for dielectric elastomers. The driving strain (s) of the dielectric elastomers can be calculated according to a formula proposed by Pelrine [15]:

$$s = \frac{\varepsilon\varepsilon_0}{Y}E^2 \tag{1}$$

where Y is the elastic modulus, ε is the dielectric constant of the material, ε_0 is the vacuum permittivity (8.85×10^{-12} F/m) and E is the applied electric field strength. Therefore, it is a feasible method to obtain high driving strain under a lower electric field strength through increasing the dielectric constant of the material. A common method of increase the dielectric constant is to add ceramic fillers with high dielectric constant such as TiO_2 [16], boron nitride (BN) [17], and $PbZr_{0.52}Ti_{0.48}O_3$ [18] into the polymer matrix. However, in order to obtain a high dielectric constant, it is necessary to add a higher volume fraction of ceramic filler, resulting in low breakdown voltage, high elastic modulus and poor processing performance, which greatly limits the application of dielectric elastomer. According to the percolation theory, another method of increase the dielectric constant is to add conductive fillers such as polyaniline [19,20], carbon nanotubes (CNTs) [21], and reduced graphene oxide (RGO) [22–24] into the polymer matrix. Graphene is a carbon nanomaterial with a special two-dimensional planar structure of the large specific surface area and excellent physical properties, such as thermal conductivity and

---

* Corresponding author.
E-mail address: wjw_msc@nuaa.edu.cn (J.-W. Wang).

https://doi.org/10.1016/j.eurpolymj.2021.110418
Received 19 November 2020; Received in revised form 25 February 2021; Accepted 18 March 2021
Available online 23 March 2021

electrical conductivity [25,26]. It has become a suitable and ideal candidate for the preparation of high-dielectric constant composites [27]. However, owing to strong van der Waals forces among graphene sheets, graphene sheets tend to agglomerate, and graphene has poor compatibility with the AE matrix, resulting in the formation of low dielectric constant and high dielectric loss, so it is significant to modify graphene [28].

There are generally two methods to modify graphene: non-covalent modification [29–31] and covalent modification [32,33]. Non-covalent modification is to coat a layer of organics on the surface of graphene through physical action (π–π interaction, electrostatic force, hydrogen bond, etc.) between graphene and organics, so as to achieve the purpose of improving dispersibility and inhibiting agglomeration. Compared to covalent modification, non-covalent graphene modification can maintain the intrinsic π-conjugated structure of graphene, ensuring that graphene has excellent conductivity. Lv et al. [20] used de-doped PANI to modify the exfoliated graphene nanoplates (xGNPs) through in-situ polymerization, and the obtained hybrid filler xGNPs@PANI was added to the matrix of oxidized styrenebutadienestyrene copolymer (SBS-FH) to prepare xGNPs@PANI/SBS-FH composites. The dielectric constant and dielectric loss of xGNPs@PANI/SBS-FH composite near percolation threshold filled with 9.38 vol% xGNPs@PANI were 92 and 1.01 at 100 Hz, respectively.

In this work, we use styrene and Methacryloxyethyltrimethyl ammonium chloride cationic monomer (DMC) as comonomers to prepare polystyrene cationic microspheres (referred to as PS-DMC). Through electrostatic interaction, the positively charged PS-DMC is adsorbed to the negatively charged graphene oxide (GO) in the aqueous solution (GO was highly negatively charged owing to the hydroxyls and carboxylic acid functional groups on the basal planes). Then, hydrazine hydrate was added to reduce graphene to obtain modified conductive filler PS-RGO. PS-DMC as an insulating layer can not only reduce the agglomeration of RGO sheets, but also improve the compatibility of RGO and AE (the synthetic monomer of AE used in this study contains styrene). Moreover, the non-covalent modification of RGO by PS-DMC can maintain the intrinsic π-conjugated structure of graphene, ensuring that graphene has excellent conductivity. Finally, the composites of RGO/AE and PS-RGO/AE with different content of fillers were prepared using the method of solution casting. The experimental results show that PS-RGO hybrid filler has better compatibility and dispersibility in the AE matrix than RGO, which result in the higher dielectric constant of PS-RGO/AE composites. PS-RGO/AE composites have lower dielectric loss than RGO/AE, which origins that PS-RGO hybrid filler has better dispersibility in the AE matrix.

2. Experimental section

2.1. Materials

Toluene (MB, 99.5%), potassium permanganate ($KMnO_4$, AR), hydrazine hydrate (AR), sulfuric acid (H_2SO_4, 98%, AR), 2-Hydroxyethyl acrylate (HEA, 98%), n-Butyl acrylate (BA, 99%) and styrene (St, 98%) were purchased from Nanjing Chemical Reagent Co., Ltd. (China), HEA, BA, St was purified by remove polymerization inhibitor and MB is purified by vacuum distillation to remove impurities before use. Hydrogen peroxide (H_2O_2, 30%, AR), hydrochloric acid (HCl, 36–38%, AR), and anhydrous methanol (MeOH, AR) were obtained from Sinopharm Chemical Reagent Co., Ltd. (China). Natural graphite, benzoyl peroxide (BPO), and Methacryloxyethyltrimethyl ammonium chloride (DMC, AR) were purchased from Aladdin Chemistry Co., Ltd. (Shanghai, China), BPO was recrystallized before use, and DMC was purified by remove polymerization inhibitor.

2.2. Synthesis of PS-DMC and AE

The preparation of PS-DMC adopts the method of dispersion polymerization [34], as shown in Fig. 1(a). In a typical procedure, 4.545 g of St and 0.0906 g of DMC were added to the three-necked flask containing with 40 mL of methanol and 10 mL of deionized water under magnetic stirring, condensate reflux, and nitrogen atmosphere. After 5 min, 0.0906 g of initiator AIBN was added to the reaction system and the temperature was raised to 80 °C. After 8 h, the reaction was completed, and the resulting dispersion was sealed and stored in a beaker. The AE was prepared according to Ref. 7, as shown in Fig. 1(b).

2.3. Fabrication of PS-RGO

RGO was fabricated from chemical reduction after graphite is exfoliated into graphene oxide (GO) using an improved Hummers method [35]. In a typical procedure, 2 g graphite powder was added to one-necked flask with 46 mL H_2SO_4, and the mixture was magnetically stirred for 30 min under ice bath conditions. Subsequently, 6 g $KMnO_4$ was slowly added to the reaction system, followed by magnetic stirring for 2 h below 2 °C. Next, the reaction system was heated to 35 °C, and the mixture was magnetically stirred for 4 h. Finally, 92 mL of deionized water was slowly added to the reaction system to keep the temperature around 95 °C. 280 mL deionized water and 20 mL H_2O_2 were added sequentially to terminate the reaction, and a bright yellow slurry was obtained. The slurry was washed with 5% HCl three times and deionized water several times to make the pH close to 7. After ultrasonic, dialysis, and freeze-drying treatment, GO was obtained. GO was dispersed in deionized water to obtain a 1 mg/mL dispersion, and hydrazine hydrate (the mass ratio of GO and hydrazine hydrate is 1: 0.7) was added after the temperature was raised to 95 °C, and the mixture was magnetically stirred for 4 h under a nitrogen atmosphere. The reaction product is filtered, washed with deionized water, and dried to obtain RGO.

GO is decorated with PS-DMC through electrostatic interaction between them in deionized water, as shown in Fig. 2. 200 mg GO was added to three-necked flask with 200 mL of deionized water, followed by ultrasonic treatment and magnetic stirring to make it completely dispersed in water. Next, 200 mg PS-DMC emulsion was added into the graphene oxide aqueous suspension, and the suspension was magnetically stirred for 20 min. Finally, 140 mg hydrazine hydrate was added into the suspension after the temperature was raised to 95 °C, and the suspension was magnetically stirred for 4 h with refluxing under a nitrogen atmosphere. The obtained black dispersion was filtered and washed three times with deionized water, and the resulting precipitate was dried at 60 °C in a vacuum oven. The obtained product was named as PS-RGO.

2.4. Fabrication of PS-RGO/AE composites

The composite films of PS-RGO/AE were prepared using solution

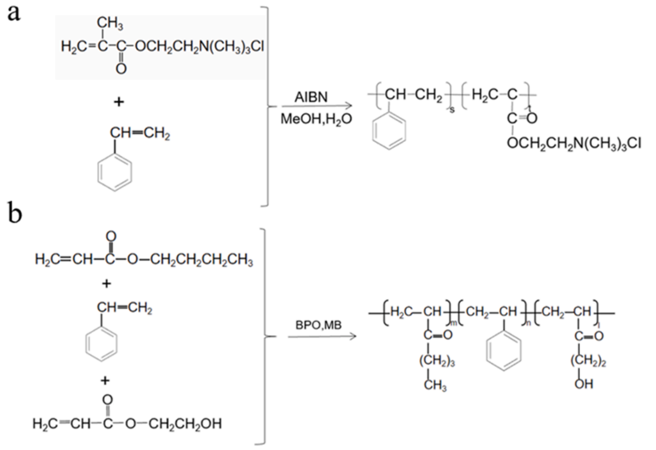

Fig. 1. Synthetic routes of (a) PS-DMC and (b) AE.

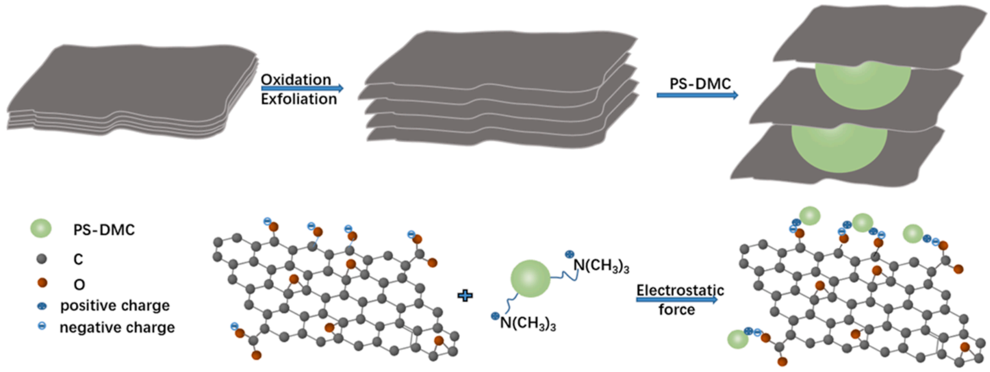

Fig. 2. Fabrication routes of PS-RGO.

casting method, as shown in Fig. S1. In detail, 0.2 g of AE was added into a beaker with 1 mL of MB, followed by magnetic stirring for 10 min. Next, PS-RGO with different volume fractions were added into the MB solution, followed by magnetic stirring for 2 h. Finally, the homogeneous dispersion was added dropwise to the glass slide and dried in air at 80 °C for 8 h, and then dried in a vacuum oven at 80 °C for 12 h. The resultant product is termed as mPS-RGO/AE, where m is the volume fraction of PS-RGO in the AE, and the values of m are 0.61, 0.91, 1.21, 1.52, 2.13, 2.43, 2.73 and 3.04%. For the purpose of comparison, the RGO/AE composite films with different volume fractions of RGO were also prepared.

2.5. Charactrization

Fourier transform infrared (FT-IR) spectra of GO, RGO, and PS-RGO were measured by using Nicolet iS50 spectrometer (Thermo Fisher), ranging from 500 to 4000 cm^{-1}. The preparation of FT-IR sample: powder samples and potassium bromide were ground under infrared light and then pressed into membrane. The Raman spectra of RGO and PS-RGO were measured with HORIBA LabRAM HR Evolution, ranging from 1200 to 2000 cm^{-1}. X-ray photoelectron spectroscopy (XPS) spectra of RGO and PS-RGO were recorded with a K-Alpha + spectrometer (Thermo Scientific) with a monochromatized Al Kα excitation source. The X-ray diffraction (XRD) pattern of RGO and PS-RGO were recorded by using a Multipupose X-ray Diffractometer (Ultima IV), ranging from 5° to 40° at 40 kV and 40 mA under ambient temperature. The microstructure of RGO and PS-RGO were observed using Transmission Electron Microscope (TEM, JEM-2100). TEM sample preparation: a proper amount of sample powder is fully dispersed in ethanol, and then dropped onto the copper mesh with a pipette, and fully dried under an Infrared light. The microstructure of RGO/AE, PS-RGO/AE composites were observed using Scanning Electron Microscope (SEM, JSM-6510). The film of the tested sample was placed in liquid nitrogen to obtain fracture surface, and the fracture surface is sprayed with gold. The DC conductivities of RGO/AE and PS-RGO/AE composites were measured using a four-probe resistivity tester (kdy-1, Guangzhou Kund Technology Co., Ltd). The dielectric properties of RGO/AE and PS-RGO/AE composites were recorded by using HP4294A precision impedance analyzer (Agilent) in the ambient temperature over the frequency range from 10^2 to 10^6 Hz. The test sample are $20 \times 20 \times 0.18\ \text{mm}^3$ rectangle films coated with circular flexible electrodes with the diameter of 3 mm. Dielectric constants (ε) of the composites were calculated according to the following formula:

$$\varepsilon = \frac{Cd}{\varepsilon_0 S} \tag{2}$$

where C, ε_0, d, S are the tested capacitance, the vacuum permittivity, the thickness of the measured composite films, and the area of the electrode painted on the composite films. The breakdown voltage was measured with a dielectric withstand voltage test (Beijing Electromechanical Research Institute, China). Dynamic mechanical properties of composites were measured by using An NBW 500 TBA (Changchun Intelligent Instrument and Equipment Co., Ltd., China). The TGA curves were recorded by NETZSCH STA409PC. Samples (about 10 mg) were sealed in Al_2O_3 pans and the testing temperature was measured from 25 °C to 600 °C at a rate of 10 °C/min. Area actuation strain measurements were performed with films stretched on a circular rigid frame and the bidirectional pre-strain was 100%. A dc high-voltage power supply (DC1784L, Zhongce electronic company Ltd., Ningbo, China) was used to induce active strains in the prestrained samples.

3. Result and discussion

3.1. Synthesis of PS-RGO

The FT-IR spectra of PS-DMC, GO, RGO, and PS-RGO are shown in Fig. 3(a). The characteristic peaks of GO functional groups appear at 3418 cm^{-1}, 1724 cm^{-1}, 1630 cm^{-1}, 1387 cm^{-1}, and 1224 cm^{-1}, which are attributed to —OH stretching vibration, C═O stretching vibration, C═C stretching vibration, C—O stretching vibration, and C—O—C stretching vibration, respectively. After reduction, the —OH vibration peak was significantly weakened, and the peaks at 1724 cm^{-1} and 1630 cm^{-1} almost disappeared, which indicates a large number of oxygen-containing groups disappeared during the chemical reduction of graphene oxide, and graphene was successfully reduced [28]. Compared to the FT-IR spectrum of RGO, PS-RGO has two sharp peaks at 758 cm^{-1}, 698 cm^{-1}, which correspond to the deformation vibration of the C—H on the benzene ring, and the peaks appearing at 1446 cm^{-1} and 1490 cm^{-1} are corresponding to the vibration of the C—C on the benzene ring. The characteristic peaks appearing at 3030 cm^{-1} are attributed to the symmetric stretching vibration of the C—H on the benzene ring, and the peaks appearing at 2849 cm^{-1} and 2920 cm^{-1} are attributed to the asymmetric stretching vibration and symmetric stretching vibration of the C—H on the CH_2 of styrene [36]. These characteristic peaks also appeared in the FT-IR spectrum of PS-DMC, suggesting that PS-RGO was successfully prepared.

The Raman spectra of RGO and PS-RGO are shown in Fig. 3(b). In the Raman spectrum of RGO, there are two strong peaks at 1349 cm^{-1} and 1582 cm^{-1}, which represent the D peak (defect and amorphous structure) and G peak (ordered sp^2 structure) of RGO, respectively. In the PS-RGO Raman spectrum, the intensity ratio of D peak and G peak (I_D/I_G) (1.12) is lower than that of RGO (1.26). The modification of graphene with PS-DMC is non-covalent, and there is no chemical interaction between them, so the I_D does not change. The decrease in I_D/I_G is caused by the π–π interaction between the polystyrene chain segments and graphene [28]. The existence of π–π interaction is favorable for the modification of RGO by PS-DMC.

The element types, element content, molecular structure and

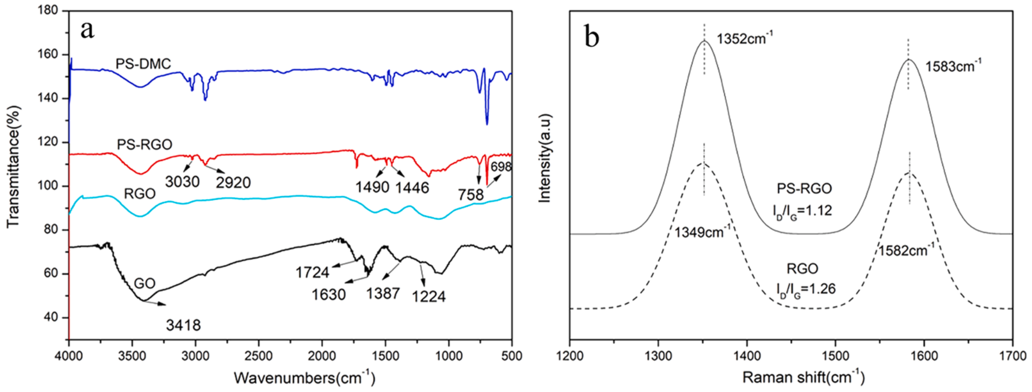

Fig. 3. FT-IR spectra of PS-DMC, GO, RGO, and PS-RGO (a). Raman spectra of RGO and PS-RGO (b).

chemical state of RGO and PS-RGO were obtained by XPS spectroscopy measurement, to determine whether PS-DMC microspheres were successfully adsorbed on the surface of RGO. As shown in Fig. S2(a), both C and O elements are present in RGO and PS-RGO. Compared with RGO, the peak intensity of C1s of PS-RGO increases, and the peak intensity of O1s decreases and PS-RGO has a higher C/O ratio (4.21) than that of RGO (2.72), which results from PS containing C element but not O element [28]. In addition, in the XPS spectrum of PS-RGO, a new element peak of N1s appears, which results from the comonomer of DMC containing N element. As shown in Fig. S2(b), the C1s peak in PS-RGO can be split into four peaks. Among them, the peak of the binding energy of 284.59 eV is corresponding to the C—C on graphene and polystyrene, and the peaks of the binding energy of 285.38 eV, 287.78 eV and 291.51 eV are corresponding to the C—O, O—C═O, C═O deriving from the oxygen-containing group on the edge of the graphene, respectively. As shown in Fig. S2(c), the O1s peak in PS-RGO can be split into two peaks. The peaks at 531.7 eV and 533.4 eV are corresponding to the C—O and C═O on graphene, respectively. As shown in Fig. S2(d), the peak at 399.95 eV is corresponding to the C—N on the PS-DMC. XPS spectroscopy results indicate that the PS-DMC microspheres were successfully adsorbed on the graphene sheets.

In order to calculate the content of PS-DMC in PS-RGO, we tested the TGA curve of RGO and PS-RGO. As shown in Fig. S3, the RGO exhibits a mass loss at 180 °C, which is attributed to the pyrolysis of retained oxygen-containing groups on RGO. And the PS-RGO exhibits two characteristic mass losses, one appears at 180 °C and the other one corresponds to the decomposition of PS-DMC at 300 °C. After calculation, the mass ratio of PS-DMC to RGO is 5:4.

3.2. *Microstructure of RGO and PS-RGO*

Graphene has a tendency to agglomerate, resulting in inhomogeneous dispersion in the matrix. Therefore, it is significant to investigate the microstructure of RGO and PS-RGO through XRD and TEM.

The XRD patterns of RGO, PS-DMC and PS-RGO are shown in Fig. 4. In the XRD patterns of RGO, a broad diffraction peak appears at $2\theta = 24.1^\circ$, and its interlayer distance (3.703 Å) is close to that of natural graphite (3.39 Å). In the XRD patterns of PS-DMC, the peak appears at $2\theta = 18.5^\circ$ is correspond to PS. Comparing the XRD patterns of RGO with PS-RGO, it is noticed that the diffraction peak shifted from 24.1° to 19.4°, which is attributed to the addition of the RGO and PS. The results of XRD also confirm the preparation of PS-RGO is successful.

TEM photographs of RGO and PS-RGO were shown in Fig. 5. As mentioned before, RGO stack and agglomerates together on account of strong van der Waals force between sheets. From the TEM images of PS-RGO, it is easily noticed that fewer layers of graphene sheets can be observed at the edge, which origins that PS-DMC acts as a spacer to increase the interlayer spacing of graphene and reduces the phenomenon of sheets agglomeration. Moreover, the existence of π–π interaction between PS-DMC and graphene weakens the van der Waals force between graphene sheets, which reduces the phenomenon of sheets agglomeration. Furthermore, the reduction of sheet agglomeration is beneficial to the dispersion of graphene in the AE matrix, which results in the improvement of dielectric properties.

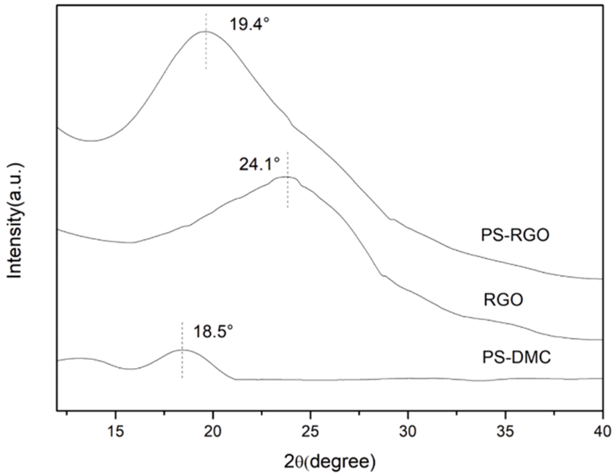

Fig. 4. XRD patterns of RGO, PS-DMC and PS-RGO.

3.3. *Microstructure of RGO /AE and PS-RGO/AE composites*

In order to more intuitively observe the dispersion of RGO and PS-RGO fillers in the AE matrix, SEM fracture surface images of the composites are essential. As shown in Fig. 6(b), RGO presents an large massive particles in the matrix, especially at the bottom of the figure. This is due to the agglomeration of RGO caused by the poor dispersibility of RGO in the AE matrix. However, As shown in Fig. 6(a), PS-RGO presents a very small layered shape in the matrix, uniformly dispersed and no obvious agglomeration. On the one hand, PS-DMC microspheres act as insulating layer to isolate graphene sheets, and the π–π interaction between PS-DMC and RGO also weakens the van der Waals force of the graphene sheets, so the agglomeration phenomenon is reduced. On the other hand, AE matrix contains styrene, which may cause the compatibility of PS-RGO with the AE matrix is better than that of RGO, so it has better dispersion in the matrix.

3.4. *Electric properties of the composites*

Fig. 7 exhibits the curve of the DC conductivity of the composites with the content of conductive filler. Overall, the conductivity of either RGO/AE or PS-RGO/AE increases with the increase of the conductive

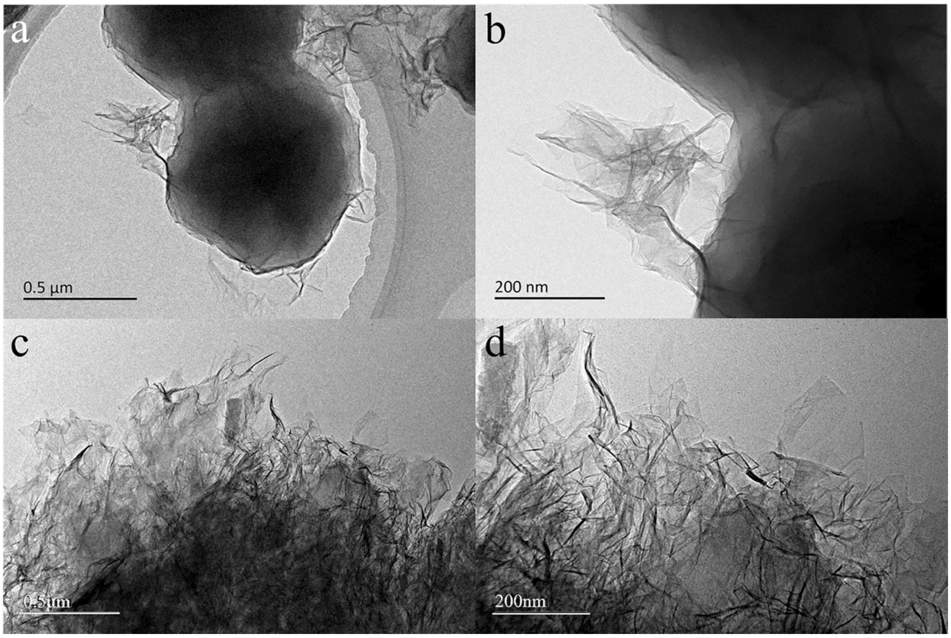

Fig. 5. TEM images of PS-RGO (a, b) and RGO (c, d).

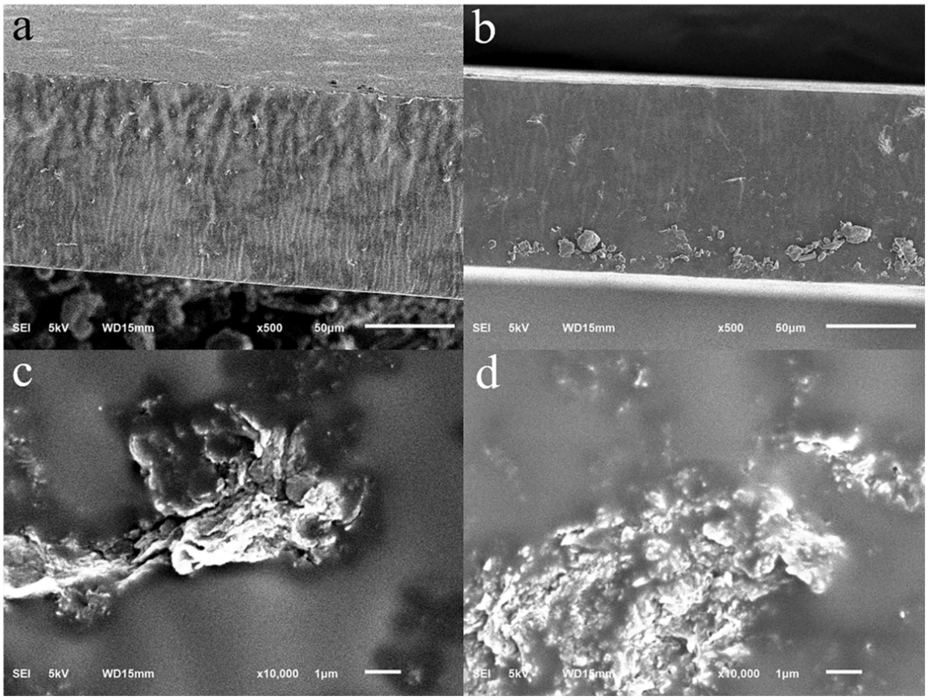

Fig. 6. SEM images of fracture surfaces of PS-RGO/AE (a, c) and RGO/AE (b, d).

filler. Specifically, when a small amount of conductive filler was added, the conductivity increases slowly, and when the filler loadings approach a critical value (percolation threshold), the conductivity increases sharply, and the composites change from an insulator to a conductor. After the content of the filler beyond the percolation threshold, the conductivity increases slowly. The above phenomenon can be explained by the percolation theory. The percolation threshold of RGO/AE and PS-RGO/AE composites can be acquired by the least-squares fit of the electrical conductivity by the following formula:

$$\sigma \propto (f_c - f)^{-s} \quad f < f_c \tag{3}$$

$$\sigma \propto (f - f_c)^{t} \quad f > f_c \tag{4}$$

where σ, f, and f_c are the DC conductivity of the composite, the volume fraction of the filler, and the percolation threshold of the composite, respectively. And t and s are the critical parameters [37]. The percolation thresholds of RGO/AE and PS-RGO/AE composites were 1.58 vol% and 2.46 vol%, respectively, through formula fitting. PS-RGO/AE composites have a higher percolation threshold than RGO/AE composites, which results from following reasons. (1) The hybrid filler of PS-RGO has better compatibility with the AE matrix, which improves the dispersion of PS-RGO in the matrix. (2) PS-DMC microspheres act as

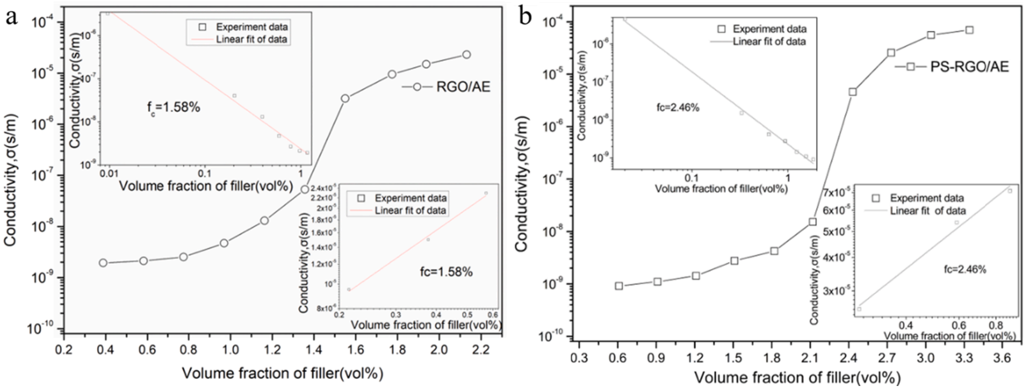

Fig. 7. The DC conductivity of RGO/AE (a) and PS-RGO/AE (b) varies with fillers loading. The insets of top left corner represents the $\log(\sigma) - \log(f_c - f)$ plot ($f < f_c$). The insets of bottom right corner shows the $\log(\sigma) - \log(f - f_c)$ plot ($f > f_c$).

insulating layer to prevent the graphene from contacting each other and delay the formation of the conductive network. (3) PS-RGO contains non-conductive component PS. From this point of view, more conductive fillers need to be added to form a conductive network.

Fig. 8 exhibits the dielectric constant of RGO/AE and PS-RGO/AE composites with different conductive filler loadings as a function of the frequency of the electric field. In general, the dielectric constant of the composites decreases with increasing frequency, and the higher the content of filler, the more obvious the downward trend. The dielectric constant of the material is determined by polarization effects, including interface polarization (Maxwell-Wagner-Sillars effect), electronic polarization, and orientation polarization, etc. The interface polarization requires longer time than orientation polarization, meanwhile the electron polarization requires a short time. At low frequency, all polarizations can keep up with the change of electrical field frequency, orientation polarization and interface polarization play a leading role, so the dielectric constant is higher. As the frequency increases, due to the existence of internal resistance of the material, the orientation polarization of the dipole gradually cannot keep up with the change of the frequency, which hardly contribute to the dielectric constant, so the dielectric constant decreases [38]. Besides, the dielectric constants of 2.43 vol% PS-RGO/AE are 194 and 151 at 100 Hz and 1000 Hz, which are 2.40 times and 2.75 times that of 1.55 vol% RGO/AE. This can be mainly attributed to the following reasons. (1) Micro capacitor effect [39]. The two adjacent graphene sheets and the matrix sandwiched between them form a micro capacitor (graphene is equivalent to the electrode and the matrix is equivalent to the insulating medium), which contribute to enhance the capacitance and dielectric constant of composites. As mentioned earlier, PS-RGO has better compatibility with the matrix, so PS-RGO can be more uniformly dispersed in the matrix, which can delay the formation of conduction path. All of these are feasible to the formation of more micro capacitors, thereby improving the storage capacity of charge and dielectric constant. (2) Maxwell-Wagner-Sillars effect [40]. When there is a large difference in electrical conductivity between filler and composite matrix, charges will accumulate at the interface, leading to interface polarization to increase the dielectric constant. Among the PS-RGO/AE composites, besides the RGO-AE interface, there are also the PS-RGO interface and the PS-AE interface, and their interface types and numbers are more abundant than the RGO/AE composites. As a result, compared with RGO/AE, PS-RGO/AE composites exhibit stronger Maxwell-Wagner-Sillars effect. (3) The good dispersion of PS-RGO in the matrix delays the percolation threshold of the material, and more fillers can be added, which bring about the formation of more interfaces and more micro capacitor structures, so 2.43 vol% PS-RGO/AE composite has a higher dielectric constant than 1.55 vol% RGO/AE composite.

Fig. 9 exhibits the dependence of the dielectric constant of RGO/AE, PS-RGO/AE composites on the content of filler at 100 Hz. The changing trend of the dielectric constant of the composite with the filler content is similar to the conductivity, and the difference is that the dielectric constant will decrease beyond the percolation threshold. If the content of nano conductive filler is at a low level, the distance of adjacent graphene sheets is too far to form the micro capacitors. When the loading of conductive filler is increased, especially close to the percolation threshold, the number of micro capacitors increases sharply and the dielectric constant increases significantly. After the content of the filler beyond the percolation threshold, the composite is transformed from an insulator to a conductor, attributing to the micro capacitor effect invalid and the dielectric constant dropping sharply.

In order to further explore the difference in the dielectric properties of RGO/AE and PS-RGO/AE composites, electrochemical impedance spectroscopy is necessary. The equivalent circuit diagram of RGO/AE

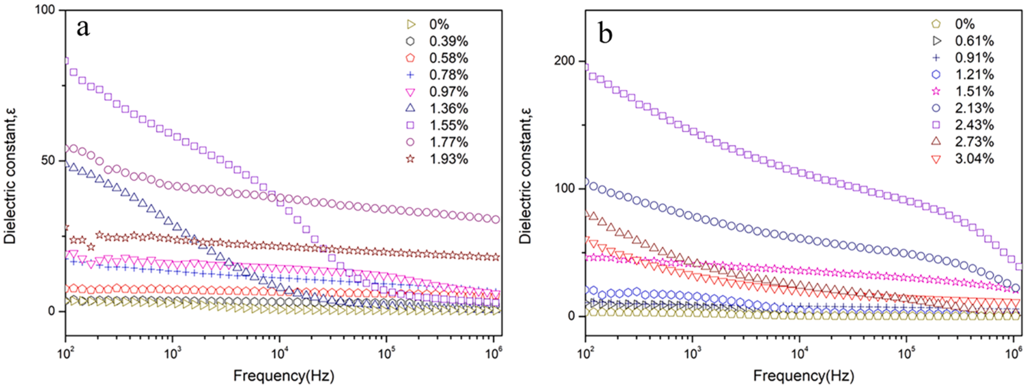

Fig. 8. Dielectric constant of RGO/AE (a) and PS-RGO/AE (b) with different volume fraction of fillers as a function of the electric field frequency.

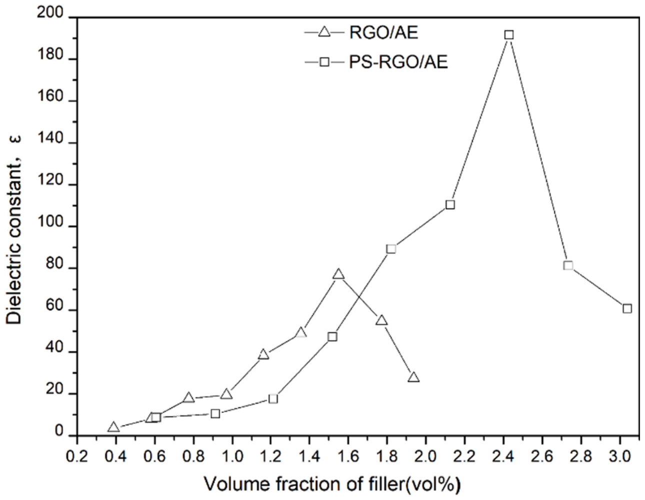

Fig. 9. Dependence of the dielectric constant of RGO/AE and PS-RGO/AE composites on the volume fraction of fillers.

and PS-RGO/AE composite materials is shown in the Fig. 10. The components of the equivalent circuit diagram of RGO/AE include substrate resistance (R_m), substrate capacitance (C_m), contact resistance (R_c), contact capacitance (C_c), charge transfer resistance (R_{ct}), and charge transfer capacitance (C_{ct}). Constant phase element (CPE) represents capacitance calibration that deviates from pure capacitive behavior. In addition to the above components in the equivalent circuit diagram of the PS-RGO/AE composites, there are also parallel resistor including polarization resistance (R_p) and CPE_p, which comes from the enhancement of the interface polarization effect. As is known to all, the semicircle diameter of Nyquist curve is related to R_{ct} for dielectric materials. According to following formula, the impedance can be considered as the synergistic effect of polarization impedance and conductivity impedance,

$$Z = Z_R + Z_P \tag{5}$$

$$Z_P = R_P + \frac{1}{jwC_P} \tag{6}$$

in which, Z_R, Z_P, R_P, j, w, and C_p represent the conductivity impedance, the polarization impedance, the polarization resistance, the imaginary unit, the angular frequency, and the polarization capacitance, respectively.

As shown in Fig. 11, the Nyquist curve of 1.77 vol% RGO/AE composites shows a typical semicircular shape, which origins from the formation of conductivity path. The Nyquist curve of 2.73 vol% PS-RGO/AE is composed of two semicircles, one of which represents R_P and another semicircle stands for the Z_R of the composite, which indicates the enhancement of dielectric constant of PS-RGO/AE composite origins from the improvement of micro capacitor effect and Maxwell-Wagner-Sillars effect. As the filler content increases, the Nyquist curve of PS-RGO/AE gradually changes from a straight line to a semicircle (Fig. S4), which demonstrates the formation of conductivity path and more micro capacitor.

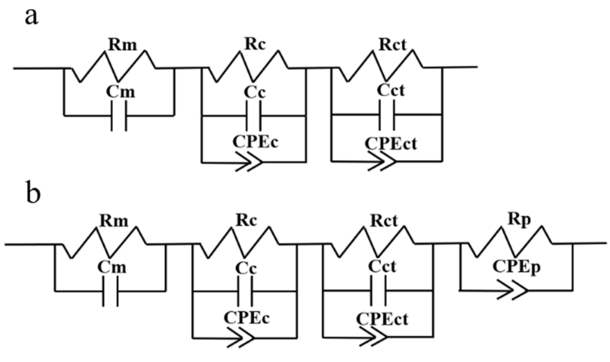

Fig. 10. The equivalent circuit diagram of RGO/AE (a) and PS-RGO/AE (b).

Fig. 12 presents the dependence of the dielectric loss of RGO/AE and PS-RGO/AE composites on the frequency of the electric field. The variation trend of the dielectric loss of the two composites is almost similar. As the frequency of the electric field increases, the dielectric loss shows a trend of falling first and then rising. To the best of our knowledge, polarization relaxation loss and conduction loss are the main causes of dielectric loss of composites. When the electric field frequency is low (such as 100 Hz), orientation polarization and interface polarization can keep up with the change of frequency. There is almost no dielectric relaxation at low frequency, and the reactive current has a negative relation with frequency, resulting in a decline of the dielectric loss at first [6]. When the electric field frequency increases to around 10^5 Hz, the internal resistance of the composites makes charge accumulation and dipole orientation more difficult. At this moment, orientation polarization and interface polarization hardly keep pace with the change of frequency, which brings about the occurrence of dielectric relaxation phenomenon and the increase of dielectric loss. In addition, compared to the dielectric loss of the composites near the percolation threshold, it is noticed that the loss of 2.43 vol% PS-RGO/AE composites at 100 Hz and 1000 Hz is 0.29 and 0.14, which are 0.25 and 0.18 times that of 1.55 vol % RGO/AE composites. As is known to all, the leakage current inside the conductor plays a significant role in the dielectric loss. Leakage current is closely related to the formation of the internal conductive network of the material, that is, it is related to the dispersion of the filler in the AE matrix. Therefore, the dielectric loss is closely related to the dispersion of the filler in the matrix. The good compatibility of PS-RGO with AE matrix leads to the homogeneous dispersion of PS-RGO in the matrix. Besides, PS-DMC acts as an insulating layer to increase the distance and suppress the leakage current between the graphene sheets. Therefore, PS-RGO/AE composites has smaller dielectric loss than RGO/AE. The PS-RGO hybrid filler in the AE matrix resulted in composite having high dielectric constant and low dielectric loss. Data given in Table S1 confirms that the PS-RGO/AE composite has better dielectric performance than the other reported similar composites.

As mentioned earlier, the polarization cannot keep up with the change of frequency at high electric field frequency, resulting in the increase of dielectric loss. PS-RGO/AE composites have dielectric relaxation under high frequency (10^6Hz), and the more filler content, the more obvious the relaxation phenomenon. This phenomenon can be depicted by the cole–cole curve, as shown in Fig. 13, which is conforming to the following revised debye formula:

$$\varepsilon * = \varepsilon_\infty + \frac{\Delta\varepsilon}{1 + (i\omega\tau)^{1-\alpha}} = \varepsilon' - i\varepsilon'' \tag{7}$$

where $\varepsilon*$ is the complex dielectric permittivity, ε' and ε'' are the real and imaginary part of $\varepsilon*$, respectively. $\Delta\varepsilon = (\varepsilon_s - \varepsilon_\infty)$, ε_s, and ε_∞ are the static dielectric constant and infinite frequency dielectric constant, respectively. α is the parameter which depicts the broadness of relaxation time, τ is the dielectric relaxation time [7]. As shown in Table 1, both ε_s and ε_∞ increase with the conductive filler added, which is consistent with the aforementioned change trend of dielectric constant with filler content. It is worth noting that the relaxation time τ will increase as the filler content increases. On the one hand, there are still defects on the surface of the reduced graphene, which act as the center of polarization and cause polarization relaxation [41]. On the other hand, the filler particles are equivalent to defects in the matrix and hinders the polarization of the dipole on the molecular chain [7]. More defects make polarization more difficult and lead to longer relaxation time.

It is significant to carry out dielectric withstanding voltage tests, which results from that the reliability of the actuator is related to the

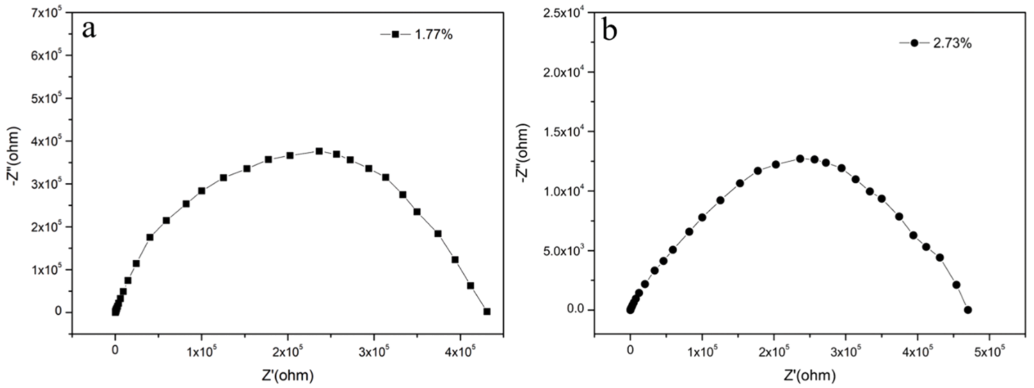

Fig. 11. The Nyquist curve of 1.77 vol% RGO/AE (a) and 2.73 vol% PS-RGO/AE (b).

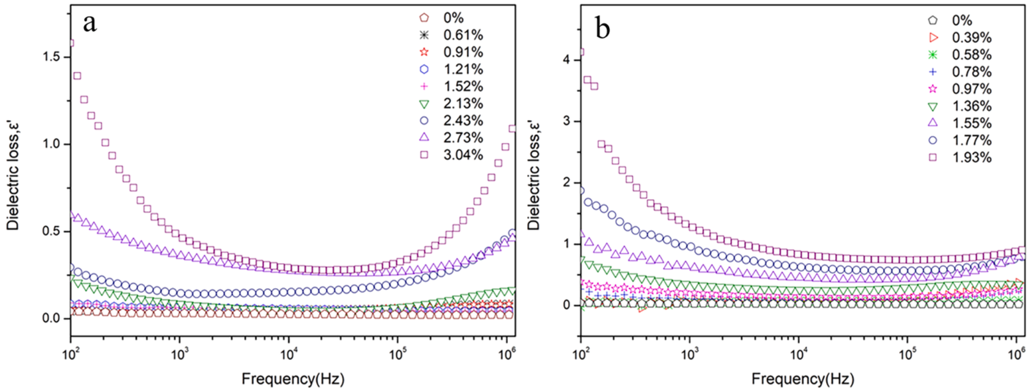

Fig. 12. Dielectric loss of PS-RGO/AE (a) and RGO/AE (b) composites with different volume fraction of fillers as a function of the electric field frequency.

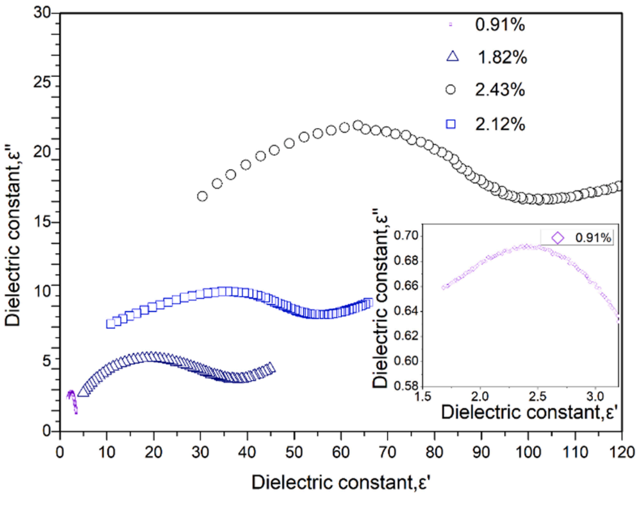

Fig. 13. The cole–cole plot of PS-RGO/AE with different volume fraction of fillers.

Table 1
The theoretical calculation data for the cole–cole plot of PS-RGO/AE.

The volume fraction of filler (vol%)	ε_s	ε_∞	τ (μs)
0.91% PS-RGO	3.76	0.86	0.027
1.82% PS-RGO	36.3	4.3	0.091
2.12% PS-RGO	53.2	17.2	0.196
2.43% PS-RGO	96.1	26.1	0.201

breakdown field strength. As shown in Table S2, the breakdown field strength of 2.43 vol% PS-RGO/AE (38.5 MV/m) is higher than that of 1.55 vol% RGO/AE (28.3 MV/m), which is attributed to improved compatibility and the more homogeneous dispersion of PS-RGO in the AE matrix.

3.5. Mechanical properties of the composites

Elastic modulus is another significant factor affecting the driving strain of the actuator. Fig. 14 shows the change of elastic modulus of

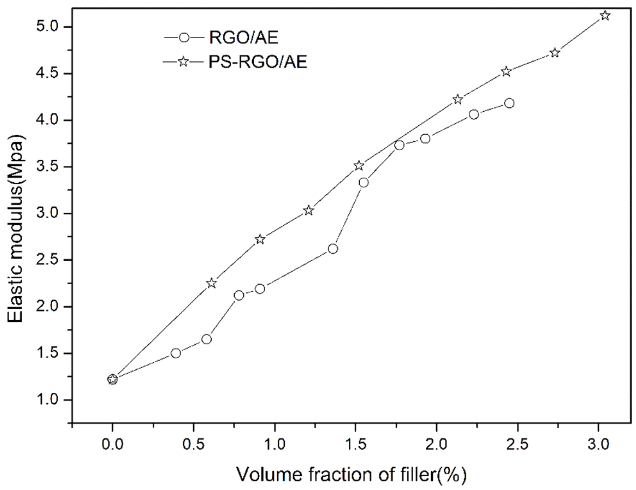

Fig. 14. Elastic modulus of RGO/AE and PS-RGO/AE composites as a function of the volume fraction of fillers.

RGO/AE and PS-RGO/AE composites with filler content. The elastic modulus of both composites increases with the increase of filler content, which results from the addition of filler hinders the movement of molecular chains. It is worth noting that the elastic modulus of PS-RGO/AE composites is higher than that of RGO/AE. The filler makes chains more rigid but in PS-RGO/AE more so because of increased compatibility between PS-RGO and AE, which brings about that the movement of the molecular chain more difficult. After the filler was added, the elastic modulus of composites is still low (the elastic modulus of 2.43 vol% PS-RGO/AE is 4.52 MPa), so it is still suitable for DE actuators.

Fig. S5 exhibits the mechanical damping (Δ) and relative rigidity ($1/p^2$) of AE and composites as function of temperature. As the temperature increases, the mechanical damping (Δ) of AE and composites appears two loss peaks, and the relative rigidity ($1/p^2$) also shows the tendency of decline in the corresponding temperature range. These two transitions correspond to different molecular motion processes of polymers. The corresponding transformation around −50 °C is a secondary transformation. In this process, the small molecular groups and chain segments of the polymer are first thawed and can move freely, which results in the decrease of relative rigidity and the appearance of loss peak. As the temperature continues to rise, the molecular chains of the polymer can also move freely, and the relative rigidity further decreases and a large loss peak appears. The corresponding temperature is the glass transition temperature Tg, and this process is the main transition (glass transition). The secondary transition temperatures of AE, 1.55 vol% RGO/AE, and 2.43 vol% PS-RGO/AE are −58.3 °C, −51.2 °C, and −45.6 °C, respectively. The glass transition temperatures of AE, 1.55% RGO/AE, and 2.43 vol% PS-RGO/AE are −19.4 °C, −15.8 °C, and −8.4 °C, respectively. The transition temperature of the composites is higher than that of the AE matrix, which origins that the addition of fillers hinders the free movement of small molecular groups and polymer molecular chains. It is worth noting that the transition temperature of PS-RGO/AE composite is higher than that of RGO/AE. The filler is equivalent to the physical cross-linking point in the matrix. PS-RGO has better compatibility with the AE matrix. Therefore, PS-RGO and the AE matrix have a stronger physical cross-linking effect, making the movement of the group and molecular chain more difficult.

3.6. *Actuated strain of RGO/AE and PS-RGO/AE*

The electromechanical sensitivity (β) was calculated based on the following equation.

$$\beta = \varepsilon / Y \tag{8}$$

As shown in Table S3, whether it is RGO/AE or PS-RGO/AE, the electromechanical sensitivity increases with the increase of filler content. This is ascribed to the increase in the dielectric constant is higher than the increase in the elastic modulus. It is worth noting that the electromechanical sensitivity of 2.43 vol% PS-RGO/AE (43.36) is higher than that of 1.55 vol% RGO/AE (24.6), which is consistent with the result of area actuation strain. As shown in Table S4, the area actuation strain of 2.43 vol% PS-RGO/AE is 18.0% at an electric field strength of 8.5 V/μm, which is higher than that of 1.55 vol% RGO/AE (3.39%). 2.43 vol% PS-RGO/AE has a higher driving strain than 1.55 vol% RGO/AE, which proves that the modification of graphene by PS-DMC is successful.

4. Conclusion

In our work, we fabricated PS-RGO/AE composites using the method of solution casting, and the PS-RGO hybrid filler was prepared by adsorbing PS-DMC to the graphene sheet through electrostatic force. PS-DMC cannot only inhibit the aggregation of graphene sheets, but also improve the dispersion of the PS-RGO hybrid filler in the AE matrix. When the filler content is close to the percolation threshold, the dielectric constant and loss of the PS-RGO/AE composites are 2.40 and 0.25 times that of the RGO/AE composites at 100 Hz. We suppose that the high dielectric constant of PS-RGO/AE results from enhanced micro capacitors effect and Maxwell-Wagner-Sillars effect through the uniform dispersion of PS-RGO in the AE matrix and the formation of more interfaces, respectively. The PS-RGO/AE composites with good dielectric and mechanical properties, which is suitable for electromechanical conversion fields.

Declaration of Competing Interest

The authors declare that they have no known competing financial interests or personal relationships that could have appeared to influence the work reported in this paper.

Acknowledgments

This work was supported by the National Natural Science Foundation of China [No. 21174063], the Aeronautical Science Foundation of China [No. 2018ZF52068], and Foundation of the Graduate Innovation Center, Nanjing University of Aeronautics and Astronautics [kfjj20180619].

Appendix A. Supplementary material

Supplementary data to this article can be found online at https://doi.org/10.1016/j.eurpolymj.2021.110418.

References

[1] Z.W. Xu, S.D. Zheng, X.T. Wu, Z.Y. Liu, High actuated performance MWCNT/Ecoflex dielectric elastomer actuatorsbased on layer-by-layer structure, Composites Part A 125 (2019) 105527.
[2] P. Elena, S. Sergiu, M.O. Dorina, Electrically Driven Artificial Muscles Using Novel Polysiloxane Elastomers Modified with Nitroaniline Push−Pull Moieties, ACS Appl. Mater. Interfaces 12 (2020) 23432–23442.
[3] Y. Ko, H. Yoon, S. Kwon, H. Lee, M. Park, I. Jeon, J.A. Lim, Elastomeric high-κ composites of low dielectric loss tangent: Experiment and simulation, Composites Part B 201 (2020) 108337.
[4] F.H. Zhou, X.X. Yang, Y.H. Xiao, Z.Q. Zhu, Electromechanic alanalysis and simplified modeling of dielectric elastomer multilayer bending actuator, AIP Adv. 10 (2020) 055003.
[5] Y. Sheima, P. Caspari, M. Dorina, Artificial muscles: dielectric elastomers responsive to low voltages, Macromol. Rapid Commun. 40 (2019) 1900205.
[6] L. Wei, J.W. Wang, X.H. Gao, H.Q. Wang, X.Z. Wang, Enhanced dielectric properties of a poly(dimethyl siloxane) bimodal network percolative composite with MXene, ACS Appl. Mater. Interfaces 12 (2020) 16805–16814.
[7] J. Shao, J.W. Wang, D.N. Liu, L. Wei, S.Q. Wu, A novel high permittivity percolative composite with modified MXene, Polymers 174 (2019) 86–95.
[8] P.S. Mahyar, A. Mahbod, N. Mina, G. Vahabodin, A. Mohammad, Programing polyurethane with rational surface-modified graphene platelets for shape memory actuators and dielectric elastomer generators, Eur. Polym. J. 133 (2020) 109745.
[9] X. Yu, Z. Lu, F. Cui, L. Cheng, Y. Cui, Tunable acoustic metamaterial with an array of resonators actuated by dielectric elastomer, Extrem. Mech. Lett. 12 (2017) 37–40.
[10] G. Moretti, G.P.R. Papini, M. Righi, D. Forehand, D. Ingram, Resonant wave energy harvester based on dielectric elastomer generator, Smart Mater. Struct. 27 (2018) 035015.
[11] P. Caspari, S.J. Dünki, F.A. Nüesch, D.M. Opris, Dielectric elastomer actuators with increased dielectric permittivity and low leakage current capable of suppressing electromechanical instability, J. Mater. Chem. C 6 (2018) 2043–2053.
[12] X. Chen, X. Pu, T. Jiang, A. Yu, L. Xu, Z.L. Wang, Tunable optical modulator by coupling a triboelectric nanogenerator and a dielectric elastomer, Adv. Funct. Mater. 27 (2017) 1603788.
[13] S. Michel, X.Q. Zhang, M. Wissler, C. Lowe, G.A. Kovacs, Comparison between silicone and acrylic elastomers as dielectric materials in electroactive polymer actuators, Polym. Int. 59 (2010) 391–399.
[14] N.Y. Ning, Q. Ma, S.T. Liu, M. Tian, L.Q. Zhang, Tailoring dielectric and actuated properties of elastomer composites by bioinspired poly(dopamine) encapsulated graphene oxide, ACS Appl. Mater. Interfaces 7 (2015) 10755–10762.
[15] R. Pelrine, R. Kornbluh, Q. Pei, J. Joseph, High-speed electrically actuated elastomers with strain greater than 100%, Science 287 (2000) 836–839.
[16] F. Carpi, D.D. Rossi, Improvement of electromechanical actuating performances of a silicone dielectric elastomer by dispersion of titanium dioxide powder, IEEE. T. Dielect. El. In. 12 (2005) 835–843.
[17] H. Fang, S.L. Bai, C.P. Wong, Thermal, mechanical and dielectric properties of flexible BN foam and BN nanosheets reinforced polymer composites for electronic packaging application, Compos. Appl. Sci. Manuf. 100 (2017) 71–80.

[18] S. Nayak, D. Khastgir, Polydimethylsiloxane PbZr0.52Ti0.48O3 nanocomposites with high permittivity: effect of poling and temperature on dielectric properties, Appl. Polymer 136 (2019) 47307.

[19] J. Shao, J.W. Wang, L. Wei, S.Q. Wu, Y.H. Yang, H. Ren, A novel high dielectric constant acrylic resin elastomer nanocomposite with pendant oligoanilines, Composites Part B 176 (2019) 107216.

[20] Q.C. Lv, Y. Li, Z.K. Zhong, H.J. Wu, F.A. He, K.H. Lam, Preparation and dielectric properties of novel composites based on oxidized styrene-butadienestyrene copolymer and polyaniline modified exfoliated graphite nanoplates, Appl. Surf. Sci. 441 (2018) 945–954.

[21] H. Sun, Interfacial polarization and dielectric properties of aligned carbon nanotubes/polymer composites: The role of molecular polarity, Compos. Sci. Technol. 154 (2018) 145–153.

[22] F. Zhang, A new low moduli dielectric elastomer nano-structured composite with high permittivity exhibiting large actuation strain induced by low electric field, Compos. Sci. Technol. 156 (2018) 151–157.

[23] M.G. Maya, J. Abraham, G. Moni, J.J. George, S.C. George, S.A. Thomas, Comprehensive study on the impact of RGO/MWCNT hybrid filler reinforced polychloroprene rubber multifunctional nanocomposites, Polym. Test. 87 (2020) 106525.

[24] N. Ning, Largely improved electromechanical properties of thermoplastic polyurethane dielectric elastomers by the synergistic effect of polyethylene glycol and partially reduced graphene oxide, Compos. Sci. Technol. 142 (2017) 311–320.

[25] M.J. Allen, V.C. Tung, R.B. Kaner, Honeycomb carbon: A review of graphene, Chem. Rev. 110 (2010) 132–145.

[26] K.Y. Shin, J.Y. Hong, S. Lee, J.J. Jang, Evaluation of antiscratch properties of graphene oxide/polypropylene nanocomposites, J. Mater. Chem. 22 (2012) 7871–7879.

[27] L.J. Romasanta, M. Hernandez, M.A. Lopez-Manchado, R. Verdejo, Functionalised graphene sheets as effective high dielectric constant fillers, Nanoscale Res. Lett. 6 (2011) 1–6.

[28] S.Q. Wu, J.W. Wang, J. Shao, L. Wei, Building a novel chemically modified polyaniline/thermally reduced graphene oxide hybrid through π-π interaction for fabricating acrylic resin elastomer-based composites with enhanced dielectric property, ACS Appl. Mater. Interfaces 9 (2017) 28887–28901.

[29] X. Ji, L. Cui, Y. Xu, J. Liu, Non-covalent interactions for synthesis of new graphene based composites, Compos. Sci. Technol. 106 (2015) 25–31.

[30] H. Wang, S.G. Bi, Y.S. Ye, Y. Xue, X.L. Xie, Y.W. Mai, An effective non-covalent grafting approach to functionalize individually dispersed reduced graphene oxide sheets with high grafting density, solubility and electrical conductivity, Nanoscale 7 (2015) 3548–3557.

[31] M. Jana, S. Saha, P. Khanra, P. Samanta, H. Koo, N.C. Murmu, T. Kuila, Non-covalent functionalization of reduced graphene oxide using sulfanilic acid azocromotrop and its application as a supercapacitor electrode material, J. Mater. Chem. A 3 (2015) 7323–7331.

[32] J.E. Johns, M.C. Hersam, Atomic covalent functionalization of graphene, Acc. Chem. Res. 46 (2013) 77–86.

[33] Y.F. Guo, F.X. Peng, H.G. Wang, F. Huang, F.B. Meng, Intercalation polymerization approach for preparing graphene/polymer composites, Polymers 10 (2018) 61.

[34] F. Zhang, Y.W. Bai, Y.H. Ma, W.T. Yang, Preparing of monodisperse and cation-charged polystyrene particles stabilized with polymerizable quarternary ammonium by dispersion polymerization in a methanol–water medium, J. Colloid Interface Sci. 334 (2009) 13–21.

[35] C.N.R. Rao, A.K. Sood, K.S. Subrahmanyam, A. Govindaraj, Graphene: The new two-dimensional nanomaterial, Angew. Chem. Int. Ed. 42 (2009) 7752–7777.

[36] T. Zhang, W.B. Huang, N. Zhang, T. Huang, J.H. Yang, Y. Wang, Grafting of polystyrene onto reduced graphene oxide by emulsion polymerization for dielectric polymer composites: High dielectric constant and low dielectric loss tuned by varied grafting amount of polystyrene, Eur. Polym. J. 94 (2017) 196–207.

[37] Z.M. Dang, Y.H. Lin, C.W. Nan, Novel ferroelectric polymer composites with high dielectric constants, Adv. Mater. 15 (2003) 1625–1629.

[38] B.K. Dash, P.G.R. Achary, N.C. Nayak, Dielectric relaxation behaviour of ethylene-vinyl acetate-exfoliated graphene nanoplatelets (xGnP) composites, J. Mater. Sci.: Mater. Electron. 26 (2015) 7244–7254.

[39] M. Jana, S. Saha, P. Khanra, P. Samanta, H. Koo, M.N. Chandra, T. Kuila, Non-covalent functionalization of reduced graphene oxide using sulfanilic acid azocromotrop and its application as a supercapacitor electrode material, J. Mater. Chem. A 3 (2015) 7323–7331.

[40] Q. Su, S. Pang, V. Alijani, C. Li, X. Feng, K. Mullen, Composites of graphene with large aromatic molecules, Adv. Mater. 21 (2009) 3191–3195.

[41] F. Ahmad, A.A. Sidek, A. Zulkiflfly, J.O. Suzan, M.K. Ahmad, Preparation of a chemically reduced graphene oxide reinforced epoxy resin polymer as a composite for electromagnetic interference shielding and microwave-absorbing applications, Polymers 10 (2018) 1180.